

	<p>Algorithm Theoretical Basis Document for the “Automatic Satellite Image Interpretation – Next Generation” Processor of the NWC/GEO MTG-I day-1</p>	<p>Code:NWC/CDOP2/MTG/ZAMG/SCI/ATBD/ASII-NG Issue: 1.1.1 Date: 31 March 2025 File:NWC-CDOP2-MTG-ZAMG-SCI-ATBD-ASII-NG_v1.1.1 Page: 1/26</p>
---	---	---



Algorithm Theoretical Basis Document for the “Automatic Satellite Image Interpretation – Next Generation” Processor of the NWC/GEO MTG-I day-1

NWC/CDOP2/MTG/ZAMG/SCI/ATBD/ASII-NG, Issue 1.1.1

31 March 2025

Applicable to

GEO-ASII-NG v2025 (NWC-049)

which is comprised of

GEO-ASII-TF-v3.0

GEO-ASII-GW-v2.0

GEO-ASII-ICE-v1.0

Prepared by GeoSphere Austria

	<p>Algorithm Theoretical Basis Document for the “Automatic Satellite Image Interpretation – Next Generation” Processor of the NWC/GEO MTG-I day-1</p>	<p>Code:NWC/CDOP2/MTG/ZAMG/SCI/ATBD/ASII-NG Issue: 1.1.1 Date: 31 March 2025 File:NWC-CDOP2-MTG-ZAMG-SCI-ATBD-ASII-NG_v1.1.1 Page: 2/26</p>
---	---	---

REPORT SIGNATURE TABLE

Function	Name	Signature	Date
Prepared by	A. Jann, I. Meirold-Mautner & A. Wirth (ZAMG)		<i>31 March 2025</i>
Revised by	A. Jann, I. Meirold-Mautner & A. Wirth (ZAMG)		<i>31 March 2025</i>
Reviewed by	A. Jann (GeoSphere Austria)		<i>31 March 2025</i>
Authorised by	Pilar Rípodas SAFNWC Project Manager		<i>31 March 2025</i>

	<p>Algorithm Theoretical Basis Document for the “Automatic Satellite Image Interpretation – Next Generation” Processor of the NWC/GEO MTG-I day-1</p>	<p>Code:NWC/CDOP2/MTG/ZAMG/SCI/ATBD/ASII-NG Issue: 1.1.1 Date: 31 March 2025 File:NWC-CDOP2-MTG-ZAMG-SCI-ATBD-ASII-NG_v1.1.1 Page: 3/26</p>
---	---	---

DOCUMENT CHANGE RECORD

Version	Date	Pages	CHANGE(S)
1.0	29 November 2013	15	Initial version, for the SAFNWC/MSG release 2015.
1.1	15 October 2016	23	Updated version, for the actual NWC/GEO release 2016.
2.0d	15 December 2016	22	Updated version, for the PCR of NWC/GEO release 2018.
1.0 (MTG)	12 January 2017	26	First version for the MTG-I PDCR.
1.1	13 November 2020	26	Update for MTG-I STRR
1.1.1	31 March 2025	26	Minor editorial changes and updates in output format, for first MTG-I1 release

	Algorithm Theoretical Basis Document for the “Automatic Satellite Image Interpretation – Next Generation” Processor of the NWC/GEO MTG-I day-1	Code: NWC/CDOP2/MTG/ZAMG/SCI/ATBD/ASII-NG Issue: 1.1.1 Date: 31 March 2025 File: NWC-CDOP2-MTG-ZAMG-SCI-ATBD-ASII-NG_v1.1.1 Page: 4/26
---	--	--

Table of contents

1. INTRODUCTION	6
1.1 SCOPE OF THE DOCUMENT	6
1.2 SOFTWARE VERSION IDENTIFICATION	6
1.3 IMPROVEMENTS SINCE THE PREVIOUS RELEASE	6
1.4 DEFINITIONS, ACRONYMS AND ABBREVIATIONS	6
1.5 REFERENCES	7
1.5.1 <i>Applicable Documents</i>	7
1.5.2 <i>Reference Documents</i>	7
2. AUTOMATIC SATELLITE IMAGE INTERPRETATION NEXT GENERATION (ASII-NG) – OVERVIEW	9
2.1 AREAS WITH RISK OF CLEAR-AIR TURBULENCE (CAT)	9
2.2 IN-FLIGHT ICING POTENTIAL	9
3. ALGORITHM DESCRIPTION.....	10
3.1 THEORETICAL DESCRIPTION	10
3.1.1 <i>Physics of the problem</i>	10
3.1.1.1 Turbulence	10
3.1.1.2 In-flight icing	12
3.1.2 <i>Mathematical description of the algorithm</i>	14
3.1.2.1 Logistic regression	14
3.1.2.2 ASII-TF	14
3.1.2.3 ASII-GW	15
3.1.2.4 ASII-ICE	19
3.2 PRACTICAL CONSIDERATIONS	20
3.2.1 <i>Validation</i>	20
3.2.2 <i>Quality control and diagnostics</i>	21
3.2.3 <i>Description of the output</i>	21
4. ASSUMPTIONS AND LIMITATIONS	23
5. REFERENCES	24
ANNEX 1: ANCILLARY DATA	26

	<p>Algorithm Theoretical Basis Document for the “Automatic Satellite Image Interpretation – Next Generation” Processor of the NWC/GEO MTG-I day-1</p>	<p>Code:NWC/CDOP2/MTG/ZAMG/SCI/ATBD/ASII-NG Issue: 1.1.1 Date: 31 March 2025 File:NWC-CDOP2-MTG-ZAMG-SCI-ATBD-ASII-NG_v1.1.1 Page: 5/26</p>
---	---	---

List of Tables and Figures

Table 1: List of Applicable Documents.....	7
Table 2: List of Referenced Documents.....	8
Table 3: Risk of icing due to supercooled water droplets in dependence of temperature and cloud type (following the Aircraft Icing Handbook, 2000).....	12
Table 4: Input parameters from NWP and satellite data for the detection of tropopause folds	15
Figure 1: Schematic of a tropopause fold.....	10
Figure 2: Graphical representation of two Gabor filter functions used in the gravity wave detection. (a) $\gamma=0.4$, $\sigma=2.0$, $\lambda=5$, $\Theta=13\pi/16$, $\varphi=0$, (b) $\gamma=0.4$, $\sigma=2.8$, $\lambda=7$, $\Theta=7\pi/16$, $\varphi=\pi$	16
Figure 3: Schematic of the grating detection. In principle, the situation is evaluated at the dots in equidistant spacing, but as one often lies at the edge of pixels, a tolerance is applied and the four closest pixels are examined. As the pixel at the centre of the search line has a Gabor value typical for a white stripe, the pixels marked with the blue triangles are checked for being characteristic for white stripes, whereas at least one in each red-triangle group should show a strong dark-stripe signal.	18

	Algorithm Theoretical Basis Document for the “Automatic Satellite Image Interpretation – Next Generation” Processor of the NWC/GEO MTG-I day-1	Code: NWC/CDOP2/MTG/ZAMG/SCI/ATBD/ASII-NG Issue: 1.1.1 Date: 31 March 2025 File: NWC-CDOP2-MTG-ZAMG-SCI-ATBD-ASII-NG_v1.1.1 Page: 6/26
---	--	--

1. INTRODUCTION

1.1 SCOPE OF THE DOCUMENT

This document is the Algorithm Theoretical Basis Document for the “Automatic Satellite Image Interpretation – Next Generation” (ASII-NG) / PGE 17 of the NWC/GEO software package.

This document contains a description of the algorithms, including scientific aspects and practical considerations.

1.2 SOFTWARE VERSION IDENTIFICATION

This document describes the algorithms implemented in the PGE 17 version for the NWC/GEO software package delivery at MTG-I day-1. The PGE has three sub-modules: the detection of tropopause foldings, ASII-TF v3.0, the detection of gravity wave patterns, ASII-GW v2.0 and the detection of in-flight icing potential, ASII-ICE v1.0.

1.3 IMPROVEMENTS SINCE THE PREVIOUS RELEASE

Based on accumulated CDOP-3 experience, a clearer vision on algorithms to be exploited is presented.

1.4 DEFINITIONS, ACRONYMS AND ABBREVIATIONS

ASII	Automatic Satellite Image Interpretation
ASII-GW	Gravity wave detection sub-product of ASII-NG
ASII-ICE	Icing potential sub-product of ASII-NG
ASII-NG	ASII next generation
ASII-TF	Tropopause folding detection sub-product of ASII-NG
BT	Brightness Temperature
CAT	clear air turbulence
CMIC	Cloud microphysics
COT	Cloud Optical Thickness
CTH	Cloud Top Height
CTT	Cloud Top Temperature
CTTH	Cloud Top Temperature and Height
FCI	Flexible Combined Imager
HRV	High Resolution Visible
HRW	High Resolution Winds
IR	InfraRed
IWP	Ice Water Path
LWP	Liquid Water Path

	Algorithm Theoretical Basis	Code:NWC/CDOP2/MTG/ZAMG/SCI/ATBD/ASII-NG
	Document for the “Automatic Satellite Image Interpretation – Next Generation” Processor of the NWC/GEO MTG-I day-1	Issue: 1.1.1 Date: 31 March 2025 File:NWC-CDOP2-MTG-ZAMG-SCI-ATBD-ASII-NG_v1.1.1 Page: 7/26

NWP	Numerical Weather Prediction
PIREP	Pilot Report
RDT-CW	Rapidly Developing Thunderstorms – Convection Warning
REF	Reflectivity
SEVIRI	Spinning Enhanced Visible and Infra-Red Imager
SLW(P)	Super-cooled Liquid Water (Path)
VIS	visible
WV	water vapour
ZAMG	Zentralanstalt für Meteorologie und Geodynamik

1.5 REFERENCES

1.5.1 Applicable Documents

The following documents, of the exact issue shown, form part of this document to the extent specified herein. Applicable documents are those referenced in the Contract or approved by the Approval Authority. They are referenced in this document in the form [AD.X]

For dated references, subsequent amendments to, or revisions of, any of these publications do not apply. For undated references, the current edition of the document referred applies.

Current documentation can be found at the NWC SAF Helpdesk at: <http://www.nwc-saf.eumetsat.int>.

Ref	Title	Code	Vers	Date
[AD.1]	Proposal for the Fourth Continuous Development and Operations Phase (CDOP 4) March 2022 – February 2027	/NWC/SAF/AEMET/MGT/CDOP4Proposal	1.0	12/03/21
[AD.2]	Project Plan for the NWCSAF CDOP4 phase	NWC/CDOP4/SAF/AEMET/MGT/PP	3.0.0	21/10/24
[AD.3]	Configuration Management Plan for the NWCSAF	NWC/CDOP4/SAF/AEMET/MGT/CMP	1.2.0	29/03/24
[AD.4]	System Verification and Validation Plan for the NWC/GEO MTG-I day-1	NWC/CDOP2/MTG/AEMET/MGT/SVVP	1.1	12/02/18
[AD.5]	System and Components Requirements Document for the NWC/GEO MTG-I day-1	NWC/CDOP2/MTG/AEMET/SW/SCRD	1.3.1	31/03/25
[AD.6]	Interface Control Document for Internal and External Interfaces of the NWC/GEO MTG-I day-1	NWC/CDOP2/MTG/AEMET/SW/ICD/1	1.4.0	31/03/25
[AD.7]	Interface Control Document for the NWCLIB of the NWC/GEO MTG-I day-1	NWC/CDOP2/MTG/AEMET/SW/ICD/2	1.4.0	31/03/25
[AD.8]	Data Output Format for the NWC/GEO MTG-I day-1	NWC/CDOP2/MTG/AEMET/SW/DOF	1.4.0	31/03/25
[AD.9]	Architecture Design Document for the NWC/GEO MTG-I day-1	NWC/CDOP2/MTG/AEMET/SW/ACDD	1.3.0	31/03/25
[AD.10]	SAF Level 2 Products Generation and Dissemination Baseline for MTG - [L2SAF]	EUM/PPS/DOC/09/0032		

Table 1: List of Applicable Documents

1.5.2 Reference Documents

The reference documents contain useful information related to the subject of the project. This reference document complements the applicable documents. For dated references, subsequent amendments to, or revisions of, any of these publications do not apply. For undated references, the latest edition of the document referred to applies.

	Algorithm Theoretical Basis Document for the "Automatic Satellite Image Interpretation – Next Generation" Processor of the NWC/GEO MTG-I day-1	Code: NWC/CDOP2/MTG/ZAMG/SCI/ATBD/ASII-NG Issue: 1.1.1 Date: 31 March 2025 File: NWC-CDOP2-MTG-ZAMG-SCI-ATBD-ASII-NG_v1.1.1 Page: 8/26
---	--	--

Current documentation can be found at the NWC SAF Helpdesk at <http://www.nwc-saf.eumetsat.int>

Reference	Title	Code	Vers	Date
[RD.1]	Product User Manual for the "Automatic Satellite Image Interpretation" product (ASII, PGE10)	SAF/NWC/CDOP2/ZAMG/SCI/PU M/10	2.4.2	15/07/13
[RD.2]	Scientific and Validation Report for the "Automatic Satellite Image Interpretation – Next Generation" Processors of the NWC/GEO	NWC/CDOP3/GEO/ZAMG/SCI/V R/ASII-NG	1.0	21/01/19

Table 2: List of Referenced Documents

	Algorithm Theoretical Basis Document for the “Automatic Satellite Image Interpretation – Next Generation” Processor of the NWC/GEO MTG-I day-1	Code: NWC/CDOP2/MTG/ZAMG/SCI/ATBD/ASII-NG Issue: 1.1.1 Date: 31 March 2025 File: NWC-CDOP2-MTG-ZAMG-SCI-ATBD-ASII-NG_v1.1.1 Page: 9/26
---	--	--

2. AUTOMATIC SATELLITE IMAGE INTERPRETATION NEXT GENERATION (ASII-NG) – OVERVIEW

During the precedent phases of NWCSAF, the Automatic Satellite Image Interpretation (ASII) product has been developed to analyse satellite imagery in terms of conceptual models of atmospheric phenomena, e.g. cold fronts, warm fronts, dry intrusions, etc. It came to a point that the conceptual model method could no longer be improved (but still had shortcomings), and so it was decided for the “Next-Generation” (NG) product to employ new methods of analysis to detect selected features in satellite data. These features, having the importance to aviation in common, will be discussed in some detail in the following sections.

2.1 AREAS WITH RISK OF CLEAR-AIR TURBULENCE (CAT)

Clear-air turbulence is the turbulent movement of air masses in the absence of clouds outside the planetary boundary layer, often in the upper troposphere. CAT typically has a patchy structure and horizontal dimensions of 80-500 km in the along-wind direction and 20-100 km in the across-wind direction. Vertical dimensions of CAT are 500-1000 m, and the lifespan lies between half an hour and a day (Overeem, 2002).

Forecasts of CAT in numerical weather models are difficult to perform because the scale of the physical processes involved in turbulence is smaller than most model resolutions. Thus it is of interest here to develop a method to at least identify areas from satellite data, which show (high) risks of CAT.

As its name suggests, CAT cannot be observed directly from satellite imagery since it occurs in cloud free regions. However, there exist several indicators in the vicinity of a region of CAT which can be observed in satellite data which provide an indication that CAT is likely to occur.

2.2 IN-FLIGHT ICING POTENTIAL

Just as turbulence, icing represents a considerable threat to civil aviation. Icing on the planes’ hull (body and wings) during flight occurs when super-cooled water droplets rapidly cause intense ice build-up. Ice aggregation on the wings of airplanes leads to a degradation of the stall characteristics, reduces lift and increases the weight of the airplane. Icing can also affect the jet engine, instruments, visibility and radio communication. It can be the cause for vibrations of the propeller and even block the rudder unit.

Ice crystal icing in high altitudes also presents a threat to airplanes flying near convective weather systems (and is distinguished from the super-cooled water droplets’ freezing in the ASII-NG analyses). The main risk of encountering high ice crystal concentrations appears to be downwind from the tops of large areas of convective clouds. High altitude ice crystals will not adhere to the external airframe or protrusions from it, even though these are considerably warmer than the ambient temperature because of kinetic heating. Actually, they deposit on relatively warm surfaces within the forward part of a gas turbine engine, causing malfunction and a gradual reduction in engine thrust.

	Algorithm	Theoretical	Basis	Code: NWC/CDOP2/MTG/ZAMG/SCI/ATBD/ASII-NG
	Document for the “Automatic Image Interpretation – Next Generation” Processor of the NWC/GEO MTG-I day-1	Satellite	–	Next of the
				Issue: 1.1.1 Date: 31 March 2025
				File: NWC-CDOP2-MTG-ZAMG-SCI-ATBD-ASII-NG_v1.1.1
				Page: 10/26

3. ALGORITHM DESCRIPTION

3.1 THEORETICAL DESCRIPTION

3.1.1 Physics of the problem

At the time being, the tasks of ASII-NG are:

- 1) to detect regions potentially prone to turbulence, based on meteorological parameters and combinations thereof that are known to be indicators of turbulence,
- 2) to detect regions with high in-flight icing potential.

3.1.1.1 Turbulence

In general, CAT occurs preferentially in the following meteorological situations:

- Tropopause folds
- Gravity waves (e.g. lee waves)
- Air mass boundaries (e.g. fronts)
- Wind shear (e.g. jets)
- Convection

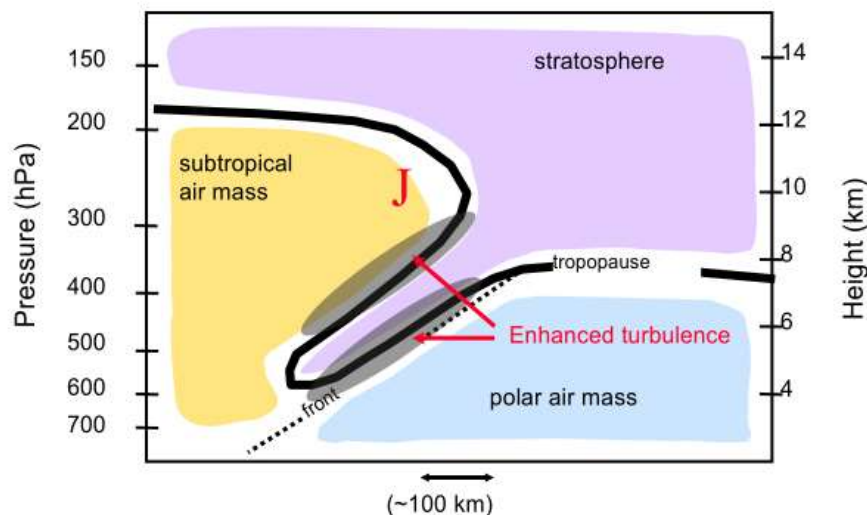


Figure 1: Schematic of a tropopause fold¹.

A tropopause fold describes the downward intrusion of stratospheric air into the troposphere, which results in a “folding” of the tropopause, as schematically illustrated in Figure 1. Typically, at a tropopause fold there is the vertical shearing at the jet stream (J) combined with the ageostrophic convergence of polar, subtropical, and stratospheric air masses. Tropopause folds mark the change in the height of the tropopause and are characterized by the occurrence of strong turbulence. Stratospheric air, which characteristically has a low moisture content and a high potential vorticity can protrude down to the mid or even the lower troposphere. Consequently,

¹ Schematic courtesy of Feltz and Wimmers, 2010: “GOES-R AWG Aviation Team: Tropopause Folding Turbulence Prediction (TFTP)”

	Algorithm Theoretical Basis Document for the “Automatic Satellite Image Interpretation – Next Generation” Processor of the NWC/GEO MTG-I day-1	Code: NWC/CDOP2/MTG/ZAMG/SCI/ATBD/ASII-NG Issue: 1.1.1 Date: 31 March 2025 File: NWC-CDOP2-MTG-ZAMG-SCI-ATBD-ASII-NG_v1.1.1 Page: 11/26
---	--	---

tropopause folds can be located by their association with gradients in upper level moisture, which are evident in the SEVIRI 6.2 μm channel sensitive to upper tropospheric water vapour. A tropopause folding turbulence product based on the ABI (Advanced Baseline Imager) sensor flown on the GOES-R series of NOAA geostationary meteorological satellites and using the 6.1 μm channel has been developed by NOAA NESDIS (Wimmers and Feltz, 2010). The tropopause height can be determined from NWP parameters such as the temperature, specific humidity or potential vorticity. The ozone content derived from SEVIRI IR channel at 9.7 μm is a good indicator for the presence of a tropopause fold (Robichaud, 2006). The lower the tropopause the more ozone is sensed by the SEVIRI instrument onboard MSG satellites. Air mass boundaries, which often coincide with tropopause folds, can be determined from satellite data. Transition zones between polar and tropical air masses are reflected in the MSG “ozone channel” IR 9.7 μm .

In the lee of mountain ridges, turbulence occurs below lee waves where a rotor cloud can develop. The turbulence cannot be directly seen, but mountain waves show the typical pattern of parallel white lines aligned perpendicular to the wind direction. Two kinds of lee waves can be discriminated: trapped lee waves, which are bound to a certain layer (due to stratification they cannot propagate across an “upper” and a “lower” border) and non-trapped lee waves, which are propagating both in vertical and horizontal directions. The energy balance is different for those two cases. For the trapped lee waves the energy of the waves is conserved within the layer – with an exchange of energy from non-turbulent to turbulent flow, whereas in the latter case energy can be transported vertically.

One criterion to estimate turbulence is the existence of a foehn gap between mountain ridge and lee clouds (Ellrod and Knox, 2010). In the case of turbulence, a pronounced sinking zone can be seen in WV, VIS and IR images. There also exists a correlation between wave length and turbulence intensity. In addition, the intensity of turbulence may be assessed by the complexity of the cloud pattern; the more complex the pattern is (e.g. crossing wave fronts) then the higher the intensity of turbulence (Uhlenbrock et al., 2007). However, these factors can probably be applied only to a very limited extent in an automatic detection tool.

Although lee clouds can be expected behind large surface elevations like mountain ranges or elevated coasts, they can also occur in lee of small hills or islands. Important for the formation of lee waves is the angle between the main wind direction and the orientation of the mountain range, and the stability of the layer of air. Ideal conditions for the appearance of lee waves occur when the air flow is near to perpendicular to the surface elevation. The wind speed ideally should exceed a certain value to allow the air flow to overflow the mountain range rather than to circulate around. In case of mountain heights up to 1000 m the wind speed should be larger than 8-10 m/s, while for higher mountain ranges, a wind speed of more than 12-15 m/s is necessary (World Meteorological Organization, 1978). An increase of the wind speed up to 20-25 m/s has shown beneficial for the development of lee waves. Lee wave development ideally occurs when the wind direction is constant with height, although variations up to 20°/ 1000m do not affect their development.

At the edge of polar fronts and in the cirrus plume associated with subtropical jets, transverse cloud bands can sometimes be observed in the IR satellite images. Turbulence at jet level originates from large vertical wind shear (Bader et al. 1995). Friction among layers with varying wind speed leads to the formation of small scale eddies (Kelvin-Helmholtz instability). Transversal cloud bands are a good indicator of turbulence at jet level.

In cases where a thermal inversion separates two layers with a marked difference in wind direction and/or speed (i.e. wind shear), gravity waves may be produced. If the wind encounters distortions at the inversion layer caused by thermals coming up from below, it will create significant shear waves in the lee of the distortions.

	Algorithm	Theoretical	Basis	Code: NWC/CDOP2/MTG/ZAMG/SCI/ATBD/ASII-NG
	Document for the “Automatic Satellite Image Interpretation – Next Generation” Processor of the NWC/GEO MTG-I day-1			Issue: 1.1.1 Date: 31 March 2025 File: NWC-CDOP2-MTG-ZAMG-SCI-ATBD-ASII-NG_v1.1.1 Page: 12/26

Turbulence is closely related to convection. Vertical mass exchanges lead to up- and downdrafts causing turbulence. However, ASII-NG intentionally does not deal with the detection of convective cells as this topic is covered elsewhere in the NWCSAF portfolio, namely in the RDT-CW product.

Algorithms developed previously to predict/analyse the occurrence of CAT were primarily based on NWP output (Ellrod and Knapp, 1991), not taking into account information provided by satellite sensors. A typical example for a turbulence warning system is the Graphical Turbulence Guidance (GTG and GTG2), developed by NCAR (Sharman et al., 2004). There currently exist a large number of numerical parameters to diagnose turbulence, but to date an all-encompassing parameter does not exist. For example, potential vorticity is critical to the detection of tropopause folds (Wimmers and Feltz, 2010); positive vorticity advection is considered to be the leading parameter in the detection of gravity waves associated with jets (transverse bandings; Knox et al., 2007); vorticity and upper level divergence are considered relevant for transverse bandings at the outflow of thunderstorms (Lenz, 2008). When considering mountain waves, characteristic numbers describing the flow, and layer stability, e.g. the Richardson Number (McCann, 2001), or some special indices developed for classifying turbulence (Ellrod Index, Brown Index, Dutton Index) are the most important measures of turbulence (Overeem, 2002). When using NWP data, the resolution of the model is crucial since turbulence is a small-scale phenomenon and is not resolved by common operational models.

3.1.1.2 In-flight icing

Conditions favourable for airframe icing have been studied extensively (e.g. World Meteorological Organization, 1954; Jeck, 2001; Ellrod and Bailey, 2006). Most icing incidents occur between 1200 and 2500 meter above ground in the temperature range of -8°C to -12°C. Ice will form on an aircraft if liquid water hits a part of the airframe, which has a temperature below freezing. Water droplets in clouds below zero degree not always turn into ice: If there are no particles around which they can form ice, water droplets can remain super-cooled down to -40°C. Super-cooled cloud droplets are most commonly found in the updraft region of cumulus clouds with temperatures below freezing down to -20°C. For temperatures below -20°C, strong ice aggregation is rarely observed, except for strong vertical motions as experienced inside thunderstorms (Sand et al., 1984; Krutina, 2006). Outside convective cells, icing conditions are found in low to mid-level stratus clouds. Nevertheless, this cloud type bears a considerable icing potential due to its larger horizontal extent. Table 3 provides an overview.

	Cumulonimbus	Stratiform clouds	Rain and drizzle
High risk	0° – -20°C	0° – -15°C	≤0°C
Medium risk	-20° – -40°C	-15° – -30°C	
Low risk	< -40°C	< -30°C	

Table 3: Risk of icing due to supercooled water droplets in dependence of temperature and cloud type (following the Aircraft Icing Handbook, 2000).

Stratiform and cumuliform cloudiness strongly differ in their icing potential. While stratiform clouds tend to have a larger horizontal extent than cumuliform clouds, they also contain rather small cloud droplets. The vertical extent of stratiform clouds is smaller than for cumuliform clouds; they show higher values of ice deposit in the upper part of the stratiform cloud. Higher cloud base temperatures go hand in hand with larger cloud water content and the icing potential therefore is larger. Icing potential in stratiform clouds is often low to moderate; nevertheless, they present a considerable threat to airplanes flying for a longer time at constant flight level.

	Algorithm Theoretical Basis Document for the “Automatic Satellite Image Interpretation – Next Generation” Processor of the NWC/GEO MTG-I day-1	Code: NWC/CDOP2/MTG/ZAMG/SCI/ATBD/ASII-NG Issue: 1.1.1 Date: 31 March 2025 File: NWC-CDOP2-MTG-ZAMG-SCI-ATBD-ASII-NG_v1.1.1 Page: 13/26
---	--	---

Stratiform clouds in higher levels (Cirrostratus, Cirrocumulus) show temperatures below -35°C and mainly consist of ice crystals.

The icing conditions are most severe for clouds consisting of super-cooled water droplets only (e.g. towering Cumulus). When water and ice phase co-exist in the same cloud (so called ‘mixed phase clouds’), the ice crystals grow rapidly on the expense of the super-cooled water droplets (Wegener-Bergeron-Findeisen process), reducing considerably the icing potential. In mixed-phase clouds, the concentration of super-cooled liquid water depends also on the humidity supply from lower levels to compensate the losses due to deposition and accretion.

To launch the Wegener-Bergeron-Findeisen process, the air temperature must be sufficiently low to activate enough cloud condensation nuclei for the formation of ice crystals. Once they have formed, ice crystals from layers on top of a liquid phase cloud can seed the lower layer of super-cooled water droplets and drastically reduce their number. Hence the top of a shower cloud which has glaciated is likely to provide less severe icing.

Large cloud droplets in combination with heavy icing conditions are found in the updraft portion of cumuliform clouds. Clear icing is most likely in building Cumulus while rime ice is often found in fully developed thunderstorms. The duration of the icing process depends on the horizontal extent of the cloud and the speed of the airplane. For Cumulus congestus, airframe icing is likely above the zero degree isotherm, showing a maximum in the upper parts of the cloud (Krutina, 2006).

Heavy icing in a very short time can be caused by freezing rain/drizzle. When rain falls through cold air, droplets become super-cooled water, which freezes on impact. Rime ice builds up rapidly and influences the aerodynamic properties of the aircraft. This extreme weather condition arises when warm and moist air overruns a layer of cold air.

From the synoptic point of view, fronts, convective systems, convergence lines and upper level lows (cold air drops) are especially prone to airframe icing. Frontal cloudiness with intense vertical motion can contain a high amount of super-cooled water below -15°C and therefore most icing incidents are located in fronts.

The largest horizontal extent of icing zones can be found within warm fronts, especially when the temperature above the frontal inversion (lifted warm air) is above 0°C and below the freezing point beneath it (cold air mass). Freezing rain ahead of the surface warm front can lead to severe icing.

Cold fronts, however, exhibit heterogeneous patterns. Vertical humidity transport is generally stronger than in warm fronts, especially in summer when convection intensifies the lifting process. In principle, icing zones are of larger vertical extent in cold fronts than in warm fronts, they are less uniform and subject to higher temporal variability.

Topographic features like mountains may alter significantly the vertical velocity of an air stream. This can result in locally changed icing conditions. The same is valid for atmospheric waves (e.g. lee waves, foehn).

While pure ice clouds such as Cirrus, Cirrostratus and Cirrocumulus represent a less significant hazard for airframe icing as they usually do not stick, so-called ‘high altitude ice crystals’ (HAIC) play an important role in in-flight icing. In mixed-phase clouds, however, when liquid cloud droplets are coating the airframe, ice crystals will freeze on the planes’ hull (pack snow).

HAIC primarily affects the gas turbine engine and strongly depends on engine geometry that favours ice accretion and aggregation of very small ice crystals (~ 40 microns) on relatively warm surfaces inside the engine, followed by their subsequent detachment and partial melting as they progress through the engine core. This process results in engine malfunction such as vibrations and even to a sudden loss of engine thrust.

	Algorithm Theoretical Basis Document for the “Automatic Satellite Image Interpretation – Next Generation” Processor of the NWC/GEO MTG-I day-1	Code: NWC/CDOP2/MTG/ZAMG/SCI/ATBD/ASII-NG Issue: 1.1.1 Date: 31 March 2025 File: NWC-CDOP2-MTG-ZAMG-SCI-ATBD-ASII-NG_v1.1.1 Page: 14/26
---	--	---

Ice crystal icing is most likely to occur in tropical latitudes where convective systems are at their most extensive. Involved ice crystals are very small and remain suspended in the atmosphere even when the convective system that produced them starts to decay. Because of their small size, they are unlikely to be detected visually and radar reflectivity is only about 5% of that of an average-sized raindrop, thus they will not appear on airborne weather radar.

Apart from droplet size, super-cooled liquid water concentration, air temperature and vertical wind speed, the airplane geometry generally plays a significant role in the icing process. Ice tends to build first on parts of the airframe with a low radius of curvature. The outer parts of the wings, sensors or door stops may well see the first indications of icing. A millimetre of ice is sufficient to affect the aerofoils. Once the icing process has started, the shape of the collecting surface is modified by the ice itself, usually in the direction that the curvature radius becomes even smaller. This leads to an even stronger ice deposition on the affected parts.

The air stream against the plane is compressed and together with friction, the air temperature rises. This effect is called aerodynamic heating, a mechanism that may suppress in-flight icing. The temperature increase due to aerodynamic heating is not uniform and depends on the plane geometry. The heating effect increases with wind speed relative to the airplane showing values of +15°C at 800 km/h. On the other side, the effects of aerodynamic heating are negligible at air speeds up to 250 km/h.

3.1.2 Mathematical description of the algorithm

3.1.2.1 Logistic regression

Ideally, the outcome of a subjective image interpretation with respect to a certain phenomenon is a binomial one, segregating the image into areas of “present” (=1) and “not present” (=0). The parameters used to arrive at that conclusion are typically continuous. A logistic regression is a possible framework to formalize that situation in a mathematical model required to attempt automatic image interpretation. As in an ordinary multiple regression, we have a dependent variable Y and several independent variables X_i tied together in a linear combination. However, the governing equation in logistic regression is somewhat more complex in order to account for the dichotomous nature of the predictand Y (P is the probability that $Y=1$):

$$\ln[P/(1-P)] = b_0 + b_1X_1 + b_2X_2 + b_3X_3 \dots$$

In order to establish the regression relation, test samples had to be collected. A sample size of 30 scenes was used, where a meteorologist subjectively encircled the regions where the phenomenon in question seemed to be present (specifically the tropopause fold as the framework is currently used in ASII-TF only). Providing these analyses and the predictands X_i for the respective scenes, regression coefficients b_i can be deduced through an iterative computation. Once this is achieved, the rest (i.e. the actual derivation of the product) is straightforward: Assemble the input data for the requested slot, compute the variables X_i and derive the probability for the presence of the phenomenon at every pixel (with the above equation solved for P).

3.1.2.2 ASII-TF

Table 4 shows the input parameters required for the detection of turbulence related to **tropopause folds**. Based on specific humidity, the height of the tropopause [hPa] is calculated from the NWP data. It is the gradient field that serves as input into the logistic regression. It is recommended that NWP data be provided up to the 50 hPa level to ensure that the tropopause is captured (on the other hand, it was found for the GFS model that the humidity fields in layers above 30 hPa are not dependable. Random fluctuations with often unrealistic increases at high levels accidentally satisfy the tropopause criteria. In order to avoid such erroneous signals, the ASII-TF software

	Algorithm	Theoretical	Basis	Code: NWC/CDOP2/MTG/ZAMG/SCI/ATBD/ASII-NG
	Document for the “Automatic Satellite Image Interpretation – Next Generation” Processor of the NWC/GEO MTG-I day-1			Issue: 1.1.1 Date: 31 March 2025 File: NWC-CDOP2-MTG-ZAMG-SCI-ATBD-ASII-NG_v1.1.1 Page: 15/26

simply omits NWP input from layers with <30hPa pressure, as the tropopause should be located in lower layers anyway).

Brightness temperature from channels IR 9.7 μm and IR 10.8 μm (FCI: 10.5, HIMAWARI: 11.2) directly serve as input, yet there are also some post-processed satellite data involved: The WV 6.2 μm (FCI: 6.3 μm) is submitted to a filter before being treated by the black stripe detection algorithm. Gradient fields are derived from WV 6.2 μm and from the brightness temperature difference of channels IR 9.7 μm and IR 10.8 μm (FCI: 10.5 μm , HIMAWARI 11.2). These gradient fields are then input into the logistic regression relation.

NWP parameter	Satellite data
specific humidity	WV 6.2 μm (SEVIRI, HIMAWARI), 6.3 μm (FCI)
wind speed at 300 hPa	IR 9.7 μm
absolute value of shear vorticity at 300 hPa	IR 10.8 μm (SEVIRI), 10.5 μm (FCI), 11.2 μm (HIMAWARI)

Table 4: Input parameters from NWP and satellite data for the detection of tropopause folds

3.1.2.3 ASII-GW

For the detection of mountain waves and transversal bandings, a method had to be implemented which can detect parallel cloud bands on meso-gamma (2-20 km) to meso-beta (20-200 km) range. The difference between the two meteorological phenomena is the circumstance that transverse banding occurs at the edge of (frontal) cloud bands at jet level while mountain waves typically appear in the low to mid troposphere and are independent of other cloud features. However, there are situations where mountain waves are embedded within fronts. In any case, the phenomena are reflected in the satellite imagery by patterns of parallel alternate dark and white stripes. For detecting them objectively, an approach advocated in a series of papers by a pair of authors (Kruizinga and Petkov, 1995, 1999; Petkov and Kruizinga, 1997) was adopted. They employed Gabor filters to identify single stripes, and subsequently applied so-called grating cell operators which looked for configurations of three stripes in equal distance. In our application, we apply the approach to the WV 7.3 and IR 10.8 channels. They can yield complementary signals, e.g. a strong argument in favour of using WV 7.3 is given by Feltz et al. (2009): the results of the vertical motions induced by gravity waves may be seen there even if the atmospheric conditions are not favourable enough for the development of clouds which is the prerequisite for identifying the gravity waves in visible and infrared bands.

The Kruizinga-Petkov model is based on Gabor filter functions $g(x, y)$ described as follows:

$$g_{\xi, \eta, \lambda, \theta, \varphi}(x, y) = \exp\left(-\frac{x'^2 + \gamma^2 y'^2}{2\sigma^2}\right) \cos\left(2\pi \frac{x'}{\lambda} + \varphi\right), \quad [1]$$

$$x' = (x - \xi)\cos\theta - (y - \eta)\sin\theta, \quad [2]$$

$$y' = -(x - \xi)\sin\theta + (y - \eta)\cos\theta, \quad [3]$$

where the parameters have the following meaning:

(ξ, η) are the coordinates of the filter centre, (x, y) are those of the pixels in the surrounding. The standard deviation σ of the Gaussian factor determines the size of the field considered around (ξ, η) (cf. parameter Ω in the following Eq. 4). The eccentricity of the filter is steered by the

	Algorithm	Theoretical	Basis	Code: NWC/CDOP2/MTG/ZAMG/SCI/ATBD/ASII-NG
	Document for the “Automatic Satellite Image Interpretation – Next Generation” Processor of NWC/GEO MTG-I day-1			Issue: 1.1.1 Date: 31 March 2025 File: NWC-CDOP2-MTG-ZAMG-SCI-ATBD-ASII-NG_v1.1.1 Page: 16/26

spatial aspect ratio γ . The parameter λ , which is the wavelength of the cosine factor, will eventually correspond to the spatial frequency of the periodic patterns detected best. The parameter $\theta \in [0, \pi)$ specifies the orientation of the normal to the parallel stripe zones (this normal is the axis x' of Eq. 2). Finally φ , the phase offset in the argument of the harmonic factor, determines the symmetry of the function. However, only symmetric filters with $\varphi=0$ and $\varphi=\pi$, respectively, will actually be used in the following. It helps in building an efficient numerical implementation to note that with a phase shift of π , the Gabor function values differ only in their signs, i.e. $g_{\xi,\eta,\lambda,\theta,\varphi=\pi}(x, y) = -g_{\xi,\eta,\lambda,\theta,\varphi=0}(x, y)$. Figure 2 offers graphical sketches of two Gabor filter matrices.

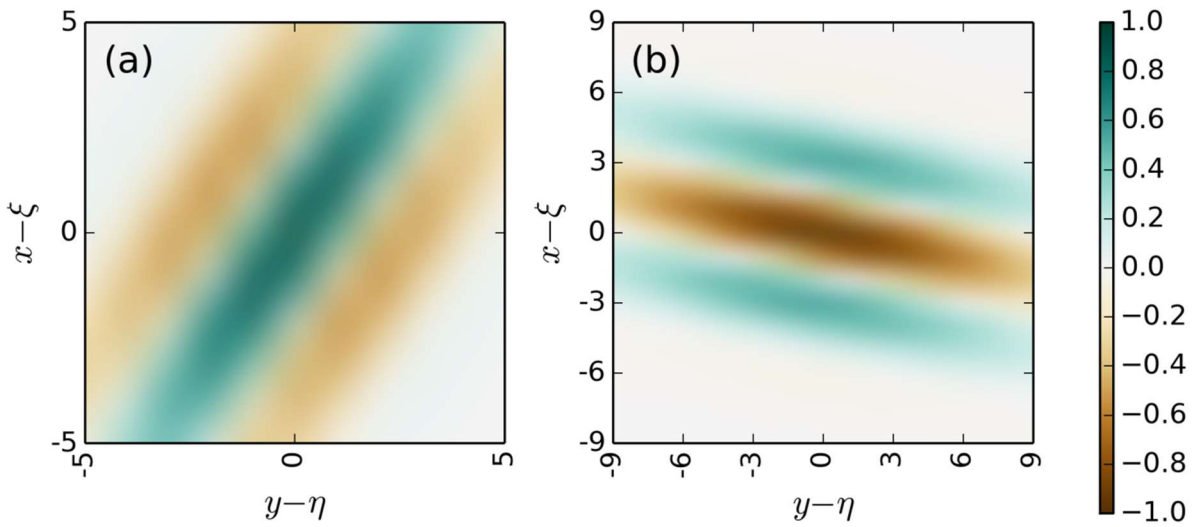


Figure 2: Graphical representation of two Gabor filter functions used in the gravity wave detection. (a) $\gamma=0.4$, $\sigma=2.0$, $\lambda=5$, $\Theta=13\pi/16$, $\varphi=0$, (b) $\gamma=0.4$, $\sigma=2.8$, $\lambda=7$, $\Theta=7\pi/16$, $\varphi=\pi$.

The filter response at any location (ξ, η) is obtained by convolving $g(x, y)$ with the WV7.3 brightness temperature image $f(x, y)$ in a vicinity Ω around (ξ, η) :

$$r_{\xi,\eta,\lambda,\theta,\varphi} = \iint_{\Omega} f(x, y) g_{\xi,\eta,\lambda,\theta,\varphi}(x, y) dx dy. \quad [4]$$

In order to make the results invariant against addition of a constant value to the input image, additional measures have to be taken. The approach discussed in Lourens (1998) was adopted where all negative values resulting from Eq. 1 are multiplied by a factor, which is obtained by summing the positive values of Eq. 1 and dividing the sum by the negative sum of the negative values. In order to preserve invariance against the sign of the image input (this symmetry is indispensable as the notion of “bright” and “dark” in imagery outside the visible spectrum is just a matter of convention), this modification of negative filter coefficients is done only for $\varphi=0$. The relation $g_{\xi,\eta,\lambda,\theta,\varphi=\pi}(x, y) = -g_{\xi,\eta,\lambda,\theta,\varphi=0}(x, y)$ remains in force and provides the Gabor function values for $\varphi = \pi$.

The values $r_{\xi,\eta,\lambda,\theta,\varphi}$ are withheld from further processing when falling below a threshold r_{min} (in other words, demanding a certain minimum response). For setting the threshold r_{min} , the convolution of the Gabor filter with an amplitude-adjusted copy of itself was computed, with the idea behind that the signal from a perfectly matching pattern with very small magnitude is assessed. This threshold magnitude is set to 0.17 K brightness temperature for MSG WV7.3 and 1.5 K for MSG IR10.8 (0.3 and 2.2 K, respectively for the corresponding channels on

	Algorithm	Theoretical	Basis	Code: NWC/CDOP2/MTG/ZAMG/SCI/ATBD/ASII-NG
	Document for the “Automatic Satellite Image Interpretation – Next Generation” Processor of the NWC/GEO MTG-I day-1			Issue: 1.1.1 Date: 31 March 2025 File: NWC-CDOP2-MTG-ZAMG-SCI-ATBD-ASII-NG_v1.1.1 Page: 17/26

MTG/Himawari/GOES-R with higher spatial resolutions and resulting sharper contrasts). In the WV analysis branch, we moreover set $r_{\xi,\eta,\lambda,\theta,\varphi}=0$ for pixels with brightness temperature below -30°C , which effectively eliminates spurious, comparatively erratic, signals from randomly matching minor water vapour fluctuations in thick cloud decks.

After having obtained $r_{\xi,\eta,\lambda,\theta,\varphi}$ for all (ξ,η) , the subsequently applied grating cell operator inspects along straight lines oriented in dependence on the angle θ . A quantity $q_{\xi,\eta,\theta,\lambda}$ is determined at all (ξ,η) :

$$q_{\xi,\eta,\theta,\lambda} = \begin{cases} 1, & \text{if } \forall n, M_{\xi,\eta,\lambda,\theta,n} \geq \rho m_{\xi,\eta,\lambda,\theta} \\ 0, & \text{if } \exists n, M_{\xi,\eta,\lambda,\theta,n} < \rho m_{\xi,\eta,\lambda,\theta}, \end{cases} \quad [5]$$

where $n \in \{-n_{max}, \dots, n_{max}\}$ (n_{max} thus defining how many adjacent stripes one wishes to find), ρ is “a threshold parameter with a value smaller than but near one” (Kruizinga and Petkov, 1995) and the auxiliary quantities $m_{\xi,\eta,\lambda,\theta}$ and $M_{\xi,\eta,\lambda,\theta,n}$ are computed as follows:

$$M_{\xi,\eta,\lambda,\theta,n} = \max\{r_{\xi',\eta',\lambda,\theta,\varphi_n} | \xi', \eta':$$

$$\left[n \frac{\lambda}{2 \cos \psi} \cos(\theta + \psi) \right] \leq (\xi' - \xi) \leq \left[n \frac{\lambda}{2 \cos \psi} \cos(\theta + \psi) \right], \quad [6]$$

$$\left[n \frac{\lambda}{2 \cos \psi} \sin(\theta + \psi) \right] \leq (\eta' - \eta) \leq \left[n \frac{\lambda}{2 \cos \psi} \sin(\theta + \psi) \right]\};$$

$$m_{\xi,\eta,\lambda,\theta} = \max\{M_{\xi,\eta,\lambda,\theta,n} | n = -n_{max}, \dots, n_{max}\} \quad [7]$$

with $[x]$ representing the floor operator (nearest integer value smaller than or equal to x) and $\lceil x \rceil$ designating the ceiling operator (nearest integer value larger than or equal to x). It is irrelevant whether the pixel at the center of the grating pattern is dark or bright. Therefore: (1) in case $r_{\xi,\eta,\lambda,\theta,\varphi=0}$ is larger than the threshold r_{min} , the test is run with $\varphi_n = 0$ for even n and $\varphi_n = \pi$ for the uneven n ; (2) if r_{min} is exceeded for $r_{\xi,\eta,\lambda,\theta,\varphi=\pi}$, the test is run with $\varphi_n = \pi$ for the even n and $\varphi_n = 0$ for the uneven values. ψ indicates that the search takes place not only orthogonal to the filter’s bars; the set of deflections used is: $-30^{\circ}, -20^{\circ}, \dots, 0, \dots, 20^{\circ}, 30^{\circ}$. Figure 3 translates formulas [6] and [7], describing the search algorithm, into a graphical representation. 8 values of θ are used, namely $\pi/16, 3\pi/16, \dots, 15\pi/16$; gravity waves exhibit an anisotropic appearance, i.e. a regularity of lines, over a larger area whereas marine stratocumulus (a potential source of false alarms in ASII-GW) are characterised over most parts by a regularity of patches. For many pixels in a Stratocumulus area, there are alternating white and black signals in a certain direction but comparably so in other, perhaps even perpendicular, directions. Consequentially, the idea is to separate the anisotropic from the isotropic cases through comparing the eight Gabor filter responses obtained for the eight values of θ at (ξ,η) for a given λ , and to retain at every pixel only the $r_{\xi,\eta,\lambda,\theta,\varphi}$ with the highest absolute value before we enter the tests [5]-[7].

The test returns a hit, signaling a grating pattern, if alternating Gabor filter signals of the same preferred orientation θ and spatial frequency $1/\lambda$ have similar magnitudes in intervals of length $\lambda/(2\cos\psi)$ along a line passing in direction $\theta + \psi$, having length $n_{max}\lambda/\cos\psi$ and being centered on point (ξ,η) . It is of course unrealistic to expect that all stripes in a satellite image look the same. Therefore, a certain tolerance is introduced into the above formulas, via parameter ρ .

	Algorithm	Theoretical	Basis	Code: NWC/CDOP2/MTG/ZAMG/SCI/ATBD/ASII-NG
	Document for the “Automatic Satellite Image Interpretation – Next Generation” Processor of the NWC/GEO MTG-I day-1			Issue: 1.1.1 Date: 31 March 2025 File: NWC-CDOP2-MTG-ZAMG-SCI-ATBD-ASII-NG_v1.1.1 Page: 18/26

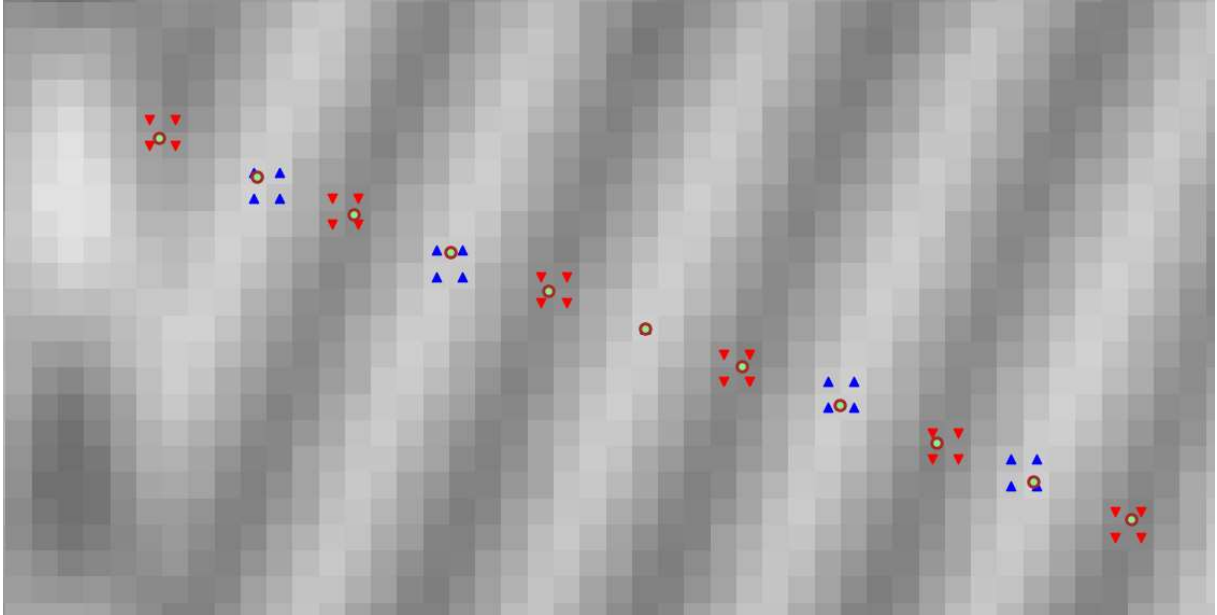


Figure 3: Schematic of the grating detection. In principle, the situation is evaluated at the dots in equidistant spacing, but as one often lies at the edge of pixels, a tolerance is applied and the four closest pixels are examined. As the pixel at the centre of the search line has a Gabor value typical for a white stripe, the pixels marked with the blue triangles are checked for being characteristic for white stripes, whereas at least one in each red-triangle group should show a strong dark-stripe signal.

In order to transform the signals $q_{\xi,\eta,\theta,\lambda}=1$ into the required “probability of gravity wave” field, one could use a distance-weighted spatial integration (similar to what was suggested in Kruizinga and Petkov (1999)):

$$w_{\xi,\eta,\theta,\lambda} = \iint_{\Omega_w} \exp\left(-\frac{(\xi-\xi')^2+(\eta-\eta')^2}{2\sigma_w^2}\right) q'_{\xi',\eta',\theta,\lambda}(x,y)d\xi'd\eta' \quad [8]$$

Integration area and standard deviation of this filter are unrelated to Eqs. 1 and 4, and in fact differ, hence the subscript w appears on Ω and σ . The motivation of introducing a new parameter q' is as follows: The q of Eq. 5, taken from the original Kruizinga-Petkov formulation, assumes 1 only for the central point of the line along which a grating pattern is detected. Yet, one can exploit the available information about extension and orientation of the phenomenon by distributing the numerical contribution of 1 evenly over that line. Therefore, $1/L$ is added to the array q' at all L pixels along the search line (as determined from the two end points through Bresenham’s (1965) line algorithm). Thus, every instance of $q=1$ equally contributes a total of 1 regardless of λ , and the results for the different wavelengths remain comparable. This is important since the computation of $w_{\xi,\eta,\theta,\lambda}$ is done separately for each tested combination of θ and λ , and the maximum density observed for any single θ - λ pair constitutes the final output at (ξ,η) . This proceeding favours regions where numerous signals are found for one specific parameter setting.

Next, the resulting maximum-density function $w_{\xi,\eta}$ is projected with a logistic function onto the (0%, 100%) range. One may regard this as a limit case of logistic regression where only one predictor variable is used. Should a future validation campaign reveal a benefit of additional predictors, they can easily be combined with the $w_{\xi,\eta}$ in the full regression framework indicated above.

It remains to list the parameter setting on which we finally settled for vMTG-I day-1, after four years of working with the algorithm: $\gamma=0.4$; $n_{max} = 5$; $\rho = 0.1$; 12 values of λ , namely 2,

	Algorithm Theoretical Basis Document for the “Automatic Satellite Image Interpretation – Next Generation” Processor of the NWC/GEO MTG-I day-1	Code: NWC/CDOP2/MTG/ZAMG/SCI/ATBD/ASII-NG Issue: 1.1.1 Date: 31 March 2025 File: NWC-CDOP2-MTG-ZAMG-SCI-ATBD-ASII-NG_v1.1.1 Page: 19/26
---	--	---

2.5...,7, 7.5 image pixels; $\sigma = 0.4 * \lambda$; $\sigma_w=5$ pixels and Ω_w is a 31×31 -pixels square. For geometrical reasons, gravity waves near the edge of the disc are not resolved by a geostationary satellite; even worse, false alarms were observed there, where pixels with very large mutual distances (in metric terms) were accidentally exhibiting regularities. Hence, an upper limit on the actually tested values of λ was introduced (a cosine function of the satellite zenith angle that assumes the value of 2 at pixels (ξ, η) with 60° zenith angle, i.e. for pixels viewed even more slantwise, no detection attempt is actually made).

Note that the evolution of the algorithm and the motivation behind some of the settings is documented in the two papers of Jann (2017, 2019), and the description here is just a technical summary of the essential algorithmic parts.

3.1.2.4 **ASII-ICE**

The current version has two modules:

- The detection of “high-altitude ice crystals”, following the algorithm proposed by de Laat et al. (2017).
- The detection of “supercooled water droplets”, following the algorithm published in Smith et al. (2012).

3.1.2.4.1 **High-altitude ice crystals (HAIC)**

The detection of high altitude ice crystals basically applies threshold levels to cloud top temperature (CTT), cloud optical thickness (COT), liquid water path (LWP) and ice water path (IWP).

The algorithm comprises the following rules:

- If the CMIC cloud phase is “liquid”, “no icing” is reported in the HAIC product
- If the CMIC cloud phase at a pixel is indicated as “ice” or “undefined”, the ASII-ICE product flags the probable presence of HAIC if the following thresholds are met:
 - $CTT < 270$ K
 - $COT > 20$
 - $LWP + IWP > 0.1$ kg/m²

(Note: these are the original values of de Laat et al. (2017). The RDT-CW developers use the algorithm to assign an ice attribute to detected convective cells, but deem a modified set of thresholds preferable ($COT > 40$, $LWP + IWP > 0.2$ kg/m²). In order to make the ASII-ICE product usable also for this application, the more demanding thresholds are also tested. If the pixel satisfies them, this is reported in the status flag for this pixel (see 3.2.3), thereby indicating an even higher certainty about HAIC occurrence.)

- In any other case (thresholds not met or some input not available), nothing is inferred about HAIC (the affected pixel receives the outage code).

3.1.2.4.2 **Supercooled water droplets**

The algorithm follows the description in Smith et al. (2012) and can be summarized as follows:

- If the CMIC cloud phase is either “undefined” or it is “ice” with a COT above 6, then the presence of super-cooled liquid water (SLW) is “unknown”. For cloud phase = “ice” with a lower COT, the result is “no icing”.
- If the CMIC cloud phase is “liquid” or “mixed”:

	Algorithm Theoretical Basis Document for the “Automatic Satellite Image Interpretation – Next Generation” Processor of the NWC/GEO MTG-I day-1	Code: NWC/CDOP2/MTG/ZAMG/SCI/ATBD/ASII-NG Issue: 1.1.1 Date: 31 March 2025 File: NWC-CDOP2-MTG-ZAMG-SCI-ATBD-ASII-NG_v1.1.1 Page: 20/26
---	--	---

- If $CTT \geq 272K$ (warm clouds) or $COT \leq 1$, no SLW should be present, the result is “no icing”
- if $CTT < 272K$ and $COT > 1$, then SLW is assumed to be present. The classification then depends on the supercooled fraction of the LWP:
 - 1) First, the freezing level is calculated from a moist adiabatic lapse rate as:

$$z_f = CTH + \frac{CTT(in^\circ C)}{0.0065}$$
 (all heights in m)
 - 2) The cloud geometrical thickness is calculated as a function of COT:

$$\Delta z(in\ m) = 390 \ln(COT) - 10$$
, with the cloud base then resulting as $z_b = CTH - \Delta z$
 - 3) Then the SLW path (SLWP) for clouds with cloud base above the freezing level is simply $SLWP = LWP$. For clouds with a cloud base below the freezing level, only a fraction of the total LWP corresponding to the sub-freezing portion is taken:

$$SLWP = LWP \times (CTH - z_f) / \Delta z.$$
 - 4) The icing probability IP is then estimated based on CMIC’s cloud top particles’ effective radius r_{eff} :

For $r_{eff} \leq 5\mu m$, one uses: $IP_5 = 0.252 \log_{10} \left(SLWP [in \frac{kg}{m^2}] \right) + 0.646$

For $r_{eff} \geq 16\mu m$, the corresponding equation reads: $IP_{16} = 0.333 \log_{10}(SLWP) + 0.984$

For values of r_{eff} in-between, the IP is determined from a linear interpolation between the two extrema: $IP = IP_5 + (IP_{16} - IP_5) \times \frac{r_{eff} - 5 \cdot 10^{-6}}{16 \cdot 10^{-6} - 5 \cdot 10^{-6}}$
 - 5) Finally, the icing severity is assigned depending on the icing probability and the LWP path:

$IP < 0.4$: low probability of light icing; $0.4 < IP \leq 0.7$: medium probability of light icing; $IP > 0.7$ and $LWP \leq 0.397\ kg/m^2$: high probability of light icing; $IP > 0.7$ and $LWP > 0.397\ kg/m^2$: high probability of medium-or-greater icing.

3.2 PRACTICAL CONSIDERATIONS

3.2.1 Validation

ASII-NG uses predefined criteria, based primarily on satellite data to detect regions favourable for turbulence. The absence of these criteria in the data does not automatically mean the absence of turbulence, since not all mechanisms of turbulence can be captured by ASII-NG (see also section 4). Thus it is not a fair measure of ASII-NG’s performance to compare its detected “fields prone to turbulence” with actual fields of turbulence, since ASII-NG can only detect a subset of all turbulent fields. Validation of ASII-NG will therefore place more emphasis on the analysis of the structures detected. This means that validation will be (at least partly) subjective by checking if the indication of a certain pattern (which is commonly accepted as related to turbulence) would be agreed by a meteorologist, too.

A verification of turbulence or icing itself is very problematic not alone due to the sparsity of available data. PIREPS (=pilot reports) could be used to check that areas recognized as being favourable for turbulence or icing by ASII-NG were indeed found to be accompanied by turbulence. The problems with that method, however, are that PIREPS just provide reports when turbulence or icing is present, with decision on issuance taken subjectively (although there are airplanes with instruments measuring vertical acceleration). Furthermore, the reports are bound to

	Algorithm Theoretical Basis Document for the “Automatic Satellite Image Interpretation – Next Generation” Processor of the NWC/GEO MTG-I day-1	Code: NWC/CDOP2/MTG/ZAMG/SCI/ATBD/ASII-NG Issue: 1.1.1 Date: 31 March 2025 File: NWC-CDOP2-MTG-ZAMG-SCI-ATBD-ASII-NG_v1.1.1 Page: 21/26
---	--	---

flight routes, thus unevenly distributed and in regions without air traffic no verification can be obtained at all. For a more comprehensive reading about difficulties of verification against PIREPs, the interested reader may like to consult the paper of Brown and Young (2000).

The approaches followed by the evaluators in this situation were somewhat different for the two sub-products ASII-GW and ASII-TF; see the validation report [RD.2] for details.

Another approach for future validation could be the use of MODE-S data. These data are generated by a combined use of ground based radar tracking and transponder data from the aircrafts. Turbulence generated by lee waves in the Alpine region has been successfully detected with MODE-S data.

3.2.2 Quality control and diagnostics

In its current version, ASII-TF cannot provide results at pixels for which one (or more) required input parameters are unavailable. The information regarding which input parameter(s) was/were missing is included as a separate flag field in the ASII-TF output file (field “asiitf_status_flag”; cf. its more detailed description in ch. 3.2.3).

ASII-GW features analyses based on WV7.3-only and/or IR10.8(10.5/11.2)-only as input, and can of course not provide a result for any invalid pixel in the respective channel. At the edges of the analysed image, vicinity evaluations as in Eqs. 6 and 8 are not possible for all θ - λ pairs; the code for “questionable” is assigned to the affected pixels in the asiigw_quality flag in order to distinguish them from the pixels where the full test battery could be run.

3.2.3 Description of the output

The ASII-NG products are encoded in standard NWCSAF netCDF output files. As such, they feature many standard entries/matrices common to all NWC/GEO netCDF products; such contents are described in the NWCSAF Data Output Format Document [AD.8]. There is one file per slot per sub-product, and the output files are located by default in \$SAFNWC/export/ASII; the naming follows the schematic S_NWC_ASII-<sub-product>_<satellite>_<region>-<resolution>_YYYYMMDDThhmmssZ.nc (examples: S_NWC_ASII-GW_MSG3_global-VISIR_20150626T120000Z.nc and S_NWC_ASII-TF_MSG3_global-VISIR_20150626T120000Z.nc).

Apart from the standard fields, the netCDF file holds the following ASII-NG-specific fields:

- (ASII-TF) “asiitf_prob”: derived probability for occurrence of tropopause folding; for each pixel a value between 0 and 100%, with failure to derive it at a certain pixel indicated by code 255.
- (ASII-TF) “asiitf_status_flag”: giving more details on reasons why “asiitf_prob” could not be derived at a certain pixel. 0=everything OK, probability computed; otherwise:
 - o bit 1 set: problem in “stripe in WV6.2”
 - o bit 2 set: problem in “(gradient in) WV6.2”
 - o bit 3 set: problem in ”gradient of the difference image IR9.7-IR10.8”
 - o bit 4 set: problem in “shear vorticity” (NWP parameter)
 - o bit 5 set: problem in “wind speed” (NWP parameter)
 - o bit 6 set: problem in “tropopause from specific humidity” (NWP parameter that may require model levels in great height)
- (ASII-GW) asiigw_pal; (ASII-TF) asiitf_pal: turquoise (0)-to-red (100%) palette

	Algorithm Theoretical Basis Document for the “Automatic Satellite Image Interpretation – Next Generation” Processor of the NWC/GEO MTG-I day-1	Code: NWC/CDOP2/MTG/ZAMG/SCI/ATBD/ASII-NG Issue: 1.1.1 Date: 31 March 2025 File: NWC-CDOP2-MTG-ZAMG-SCI-ATBD-ASII-NG_v1.1.1 Page: 22/26
---	--	---

- (ASII-GW) “asiigw_wv_prob”, “asiigw_ir_prob”: derived probability for presence of gravity wave in the WV and IR channel, respectively; for each pixel a value between 0 and 100%, with failure to derive it at a certain pixel indicated by code 255.
- (ASII-GW) “asiigw_status_flag”: giving more details on reasons why “asiigw_*_prob” could not be derived at a certain pixel. 0=everything OK, probability computed; otherwise:
 - o bit 1 set: not a valid WV7.3 pixel
 - o bit 2 set: pixel filtered by temperature threshold in WV7.3
 - o bit 3 set: not a valid IR10.8/10.5/11.2 pixel
 - o bit 4 set: pixel filtered by temperature threshold in IR10.8/10.5/11.2
- (ASII-GW) “asiigw_wv_continuity”, “asiigw_ir_continuity”: indicating the number of slots a gravity wave probability > 0% has been obtained at the pixel in the WV and IR channel, respectively, without interruption (currently testing up to 7 preceding analyses in \$SAFNWC/export/ASII; i.e. 8 being the maximum number, 1 meaning that it appeared for the first time in the current analysis).
- (ASII-ICE) “asiice_sc_mask”: flag indicating the probability of icing due to supercooled water droplets and an indication on its strength. Possible values are 0 (no icing), 1 (unknown), 2 (low probability of light icing), 3 (medium probability of light icing), 4 (high probability of light icing), 5 (high probability of medium-or-greater icing).
- (ASII-ICE) “asiice_haic_mask”: flag indicating whether icing due to high-altitude ice crystals is likely or not. Possible values are 0 (no icing), 2 (icing), 255 (product outage). Code 1 is reserved for “unknown” (to be coherent with the “asiice_sc_mask”) but currently not used.
- (ASII-ICE) “asiice_status_flag”: giving more details on the certainty about the presence of high-altitude ice crystals and reasons why “asiice_sc_mask” could not be derived at a certain pixel. 0=everything OK, probability computed; otherwise:
 - o bit 1 set: CMIC values of indicated high-altitude ice crystals even meet the more demanding thresholds of RDT-CW (for which icing is an attribute assigned to the convective cells)
 - o bit 2 set: outage of NWC/GEO CTTH input
 - o bit 3 set: outage of NWC/GEO CMIC input
- (ASII-ICE) “asiice_pal”: colour palette for icing flags

The common processing conditions and quality flags (described in [AD.8]) for these products bear the names asiigw_conditions/asiitf_conditions/asiice_conditions and asiigw_quality/asiitf_quality/asiice_quality.

	Algorithm Theoretical Basis Document for the “Automatic Satellite Image Interpretation – Next Generation” Processor of the NWC/GEO MTG-I day-1	Code: NWC/CDOP2/MTG/ZAMG/SCI/ATBD/ASII-NG Issue: 1.1.1 Date: 31 March 2025 File: NWC-CDOP2-MTG-ZAMG-SCI-ATBD-ASII-NG_v1.1.1 Page: 23/26
---	--	---

4. ASSUMPTIONS AND LIMITATIONS

These products are aimed to be part of the inputs for decision making by meteorologists, yet cannot be used as a stand-alone automatic warning tool.

The ASII-TF and ASII-GW products are satellite products searching for features favourable for turbulence but NOT the turbulence itself. As CAT by definition is a clear-air phenomenon; there may be areas of turbulence which cannot be detected by any remote-sensing tool. Therefore, the absence of signals in satellite imagery does not preclude the presence of CAT. In other words, even assuming the detection algorithms are working perfectly, the detection rate of CAT will never reach 1.

Although the NWCSAF software package can be processed at any region of the disc, the focus of tuning and validation was on Europe and the neighbouring sea areas (although the validation exercise for ASII-GW v1.0 included visits to areas on the whole disc including the southern hemisphere [RD.2]; Jann (2019)). The higher resolution of Himawari/GOES-R/MTG-FCI means that gravity waves with smaller wavelengths can be inspected. Given the typical scale of tropospheric gravity waves, this should have a positive impact on detectability. Still, for geometrical reasons, one must accept that gravity waves near the edge of the disc are not resolved or, in general terms, that the detection rate has an irremediable dependence on the satellite zenith angle.

As a consequence of the limited capabilities of sensors on geostationary satellites to scan inner-cloud microphysical processes, the icing products necessarily describe the situation only near the cloud-top level. Moreover, the detection of in-flight icing is currently confined to daylight hours as there is no Meteosat cloud microphysics product for the nighttime.

	Algorithm Theoretical Basis Document for the “Automatic Satellite Image Interpretation – Next Generation” Processor of the NWC/GEO MTG-I day-1	Code: NWC/CDOP2/MTG/ZAMG/SCI/ATBD/ASII-NG Issue: 1.1.1 Date: 31 March 2025 File: NWC-CDOP2-MTG-ZAMG-SCI-ATBD-ASII-NG_v1.1.1 Page: 24/26
---	--	---

5. REFERENCES

Aircraft Icing Handbook: Civil Aviation Authority, New Zealand, 2000. Available on the CAA web site: www.caa.govt.nz

Bader, M.J., Forbes, G.S., Grant, J.R., Lilley, R.B.E., and A.J. Waters (Eds.), 1995: Images in weather forecasting. Cambridge University Press, Cambridge.

Bresenham, J.E., 1965. Algorithm for computer control of a digital plotter. *IBM Systems Journal* 4, 25-30.

Brown, B.G., and G.S. Young, 2000: Verification of icing and turbulence forecasts: Why some verification statistics can't be computed using PIREPS. 9th Conference on Aviation, Range, and Aerospace Meteorology, Orlando, FL, 11-15 September 2000, 393-398.

de Laat, A., Defer, E., Delanoë, J., Dezitter, F., Gounou, A., Grandin, A., Guignard, A., Meirink, J. F., Moisselin, J.-M., and Parol, F., 2017: Analysis of geostationary satellite-derived cloud parameters associated with environments with high ice water content, *Atmospheric Measurement Techniques*, 10, 1359-1371, <https://doi.org/10.5194/amt-10-1359-2017>.

Ellrod G. P., and A. A. Bailey, 2006: Assessment of Aircraft Icing Potential and Maximum Icing Altitude from Geostationary Meteorological Satellite Data. *Weather and Forecasting*, 22, 160-174. doi: <http://dx.doi.org/10.1175/WAF984.1>

Ellrod G.P., and D.J. Knapp, 1991: An Objective Clear-Air Forecasting Technique: Verification and Operational Use. *Weather and Forecasting*, 7, 150-165.

Ellrod G.P., and J.A. Knox, 2010: Improvements to an Operational Clear-Air Turbulence Diagnostic Index by Addition of a Divergence Trend Term. *Weather and Forecasting*, 25, 789–798. doi: <http://dx.doi.org/10.1175/2009WAF2222290.1>

Feltz W.F., Bedka K.M., Otkin J.A., Greenwald T., and S.A. Ackerman, 2009: Understanding satellite-observed mountain-wave signatures using high-resolution numerical model data. *Weather and Forecasting*, 24, 76-86. doi: [10.1175/2008WAF2222127.1](https://doi.org/10.1175/2008WAF2222127.1).

Jann A., 2017: Detection of gravity waves in Meteosat imagery by grating cell operators. *European Journal of Remote Sensing*, 50, 509-516. <https://doi.org/10.1080/22797254.2017.1367629>

Jann, A., 2019: Objective detection of stripe patterns in satellite imagery caused by gravity waves: Lessons learnt from the southern hemisphere. *Transactions of the Royal Society of South Africa* 74, 163-172, <https://doi.org/10.1080/0035919X.2019.1596176>.

Jeck, R. K., 2001: A History and Interpretation of Aircraft Icing Intensity Definitions and FAA Rules for Operating in Icing Conditions, Office of Aviation Research, Final Report.

Knox, J.A., McCann, D.W., and P.D. Williams, 2007: Application of the Lighthill–Ford Theory of Spontaneous Imbalance to Clear-Air Turbulence Forecasting. *Journal of the Atmospheric Sciences*, 65, 3292–3304.

Kruizinga P., and N. Petkov, 1995: A computational model of periodic-pattern-selective cells. In: Mira J., Sandoval F. (Eds.), *Proc. IWANN'95, Lecture Notes in Computer Science 930*, Springer, pp. 90–99.

Kruizinga P., and N. Petkov, 1999: Nonlinear operator for oriented texture. *IEEE Transactions on Image Processing*, 8, 1395-1407. doi: [10.1109/83.791965](https://doi.org/10.1109/83.791965).

Krutina, M., 2006: Vereisung (in German), accessed in January 2016 under: http://www.wolkenschnueffler.de/media//DIR_62701/55f8ee87b0cff79ffff80e4ac144225.pdf

	Algorithm Theoretical Basis Document for the “Automatic Satellite Image Interpretation – Next Generation” Processor of the NWC/GEO MTG-I day-1	Code: NWC/CDOP2/MTG/ZAMG/SCI/ATBD/ASII-NG Issue: 1.1.1 Date: 31 March 2025 File: NWC-CDOP2-MTG-ZAMG-SCI-ATBD-ASII-NG_v1.1.1 Page: 25/26
---	--	---

Lenz, A., 2008: Identification of Transverse Band Signature in Satellite Imagery, http://www.nwas.org/committees/rs/2008_MetSat_Papers/Lenz.pdf

Lourens T., 1998: A biologically plausible model for corner-based object recognition from color images. Shaker Publishing B.V., Maastricht.

McCann, D., 2001: Gravity Waves, Unbalanced Flow and Aircraft Clear Air Turbulence. National Weather Digest, 25, 3-14.

Overeem, A., 2002: Verification of clear-air turbulence forecasts, Technisch rapport; TR-244, KNMI, De Bilt.

Petkov N., and P. Kruizinga, 1997: Computational models of visual neurons specialised in the detection of periodic and aperiodic oriented visual stimuli: bar and grating cells. Biological Cybernetics, 76, 83-96.

Robichaud, A, 2006: A case study of a remarkable tropopause folding over Eastern North America on March 14-15 2006, Technical Report, November 2006, Internal Report, https://www.researchgate.net/publication/303053095_A_case_study_of_a_remarkable_tropopause_folding_over_Eastern_North_America_on_March_14-15_2006 (accessed in February 2020).

Sand, W. R., W. A. Cooper, M. K. Politovitch, and D. L. Veal, 1984: Icing conditions encountered by a research aircraft. Journal of Climate and Applied Meteorology, 23, 1427–1440.

Sharman, R., Tebaldi, C., Wiener, G., and J. Wolff, 2006: An integrated approach to mid- and upper-level turbulence forecasting. Weather and Forecasting, 21, 268-287.

Smith W. L., Jr., P. Minnis, C. Fleeger, D. Spangenberg, R. Palikonda, and L. Nguyen, 2012: Determining the flight icing threat to aircraft with single-layer cloud parameters derived from operational satellite data. Journal of Applied Meteorology and Climatology, 51, 1794-1810.

Uhlenbrock, N.L., Bedka, K.M., Feltz, W.F., and S.A. Ackerman, 2007: Mountain Wave Signatures in MODIS 6.7µm Imagery and Their Relation to Pilot Reports of Turbulence, Weather and Forecasting, 22, 662-670.

Wimmers, A., and W. Feltz, 2010: Tropopause Folding Turbulence Product, Algorithm Theoretical Basis Document, UW/CIMSS, Version 2.0, May10, 2010. (http://www.goes-r.gov/products/ATBDs/option2/Aviation_Turbulence_v1.0_no_color.pdf).

World Meteorological Organization, 1954: Meteorological aspects of aircraft icing. WMO Tech. Note 3, WMO-30-TP9, Geneva, Switzerland, 18 pp.

World Meteorological Organization, 1978: Handbook of Meteorological Forecasting for Soaring Flights, WMO Technical Note Nr. 158.

	<p>Algorithm Theoretical Basis Document for the “Automatic Satellite Image Interpretation – Next Generation” Processor of the NWC/GEO MTG-I day-1</p>	<p>Code:NWC/CDOP2/MTG/ZAMG/SCI/ATBD/ASII-NG Issue: 1.1.1 Date: 31 March 2025 File:NWC-CDOP2-MTG-ZAMG-SCI-ATBD-ASII-NG_v1.1.1 Page: 26/26</p>
---	---	---

ANNEX 1: ANCILLARY DATA

ASII-TF makes use of the NWP fields of temperature, humidity and wind on all pressure levels listed in the central NWP configuration file (provided these levels are available in the local GRIB file)